



Hot quark matter and merger remnants

Adamu Issifu ^{1,*} and Tobias Frederico ^{1,†}

¹*Instituto Tecnológico de Aeronáutica,
CEP 12.228-900, São José dos Campos, SP, Brazil*

This work investigates hot quark matter under the thermodynamic conditions characteristic of a binary neutron star (BNS) merger remnants. We use the density-dependent quark mass model (DDQM) to access the microscopic nuclear equation of state (EoS). The strange quark matter (SQM) is studied at finite temperature and entropy in the presence of electrons and muons and their neutrinos to simulate the BNS merger conditions. We observe that as the entropy of the SQM increases, the merger remnant becomes more massive, and increases in size whereas the neutrino population also increases. In the fixed temperature case, on the other hand, we observe that the entropy spreads from the surface towards the center of the remnant. We determine the particle distribution in the remnants' core, the remnant's structure, the temperature profile, sound velocity, and the polytropic index and discuss their effects. The strange quark (SQ) remnants satisfy the $2M_{\odot}$ mass constraint associated with neutron stars (NS).

I. INTRODUCTION

The merger of two NSs leading to the detection of a gravitational wave in event GW170817 (GW) [1] results in the formation of massive remnants and subsequent matter ejection in the interstellar medium [2, 3]. The remnant comprises a central object with a massive disk around it. The characteristics of the disk and the central object depend on the masses of the merging stars, the magnetic field, NS spin, and their corresponding EoSs [4–6]. The gravitational wave was observed from the inspiral phase by Advanced LIGO [7] and Advanced Virgo [8] interferometers. This observation paved a new path into the microphysics of NSs, offering the possibility to probe matter dynamics at extreme temperature and density conditions inside these remnants. The constraint on the tidal effect of the coalescing bodies and the maximum NS mass and radii has enabled nuclear astrophysicists to impose a strict constraint on the EoS for cold NSs [9]. The detection also coincided with the observation of a γ -ray burst, GRB 170817A (GRB) [10, 11] which helps in classifying the binary contained matter using the relative time delay between the GW and GRB and the measured speed of sound [10].

Currently, gravitational waves have been observed, and future gravitational wave observatories are expected to observe more neutron star mergers with higher confidence levels. In this light, numerical simulations for the BNS merger are important to interpret the data and further constrain the EoS for NSs. Temperatures in the postmerger phase are expected to reach as high as $\sim 50 - 100$ MeV, making it suitable for finite temperature studies [12]. Even though the current gravitational wave detectors have not reported on a postmerger signal yet [1, 13, 14], however, it is expected that future detectors such as the Einstein Telescope [15] and Cosmic

Explorer [16] detectors with improved sensitivities and high-frequency features may detect BNS postmerger signals. The current sensitivity upgrades on the existing instruments also promise a better quality BNS detection with a better sky location [17].

It has been predicted through numerical relativity simulations that the final product of BNS mergers is a prompt formation of a black hole through gravitational collapse or the formation of a remnant NS [18]. In the case of NS formation, the baryon density (n_b) of a typical β -equilibrated matter of the individual NSs of about $n_b \sim 2 - 3n_0$ (n_0 is the nuclear saturation density) increases to about $n_b \sim 5 - 6n_0$ with a high remnant temperature [19–21]. A typical temperature in the postmerger remnant core at the initial stages ranges from 20 to 60 MeV [22]. This temperature further increases in the contact layer at the early stages shooting up to about 150 MeV [22, 23]. These extreme conditions are expected to be reached on shorter time scales due to the violent nature of the event, in milliseconds, under conditions relatively different from the formation of proto-NSs (PNS) through supernova remnants [24, 25]. Also, higher isospin asymmetries are expected in BNS merger events due to an excess of neutrons over protons in close binary systems NS-NS, and NS-BH [26–28], contrary to PNSs [29, 30].

Since Ivanenko and Kurdgelaideze hypothesized the existence of strange quark stars (SQSs) in 1965 [31, 32] and together with 1984 Witten's conjecture [33], namely, that SQM is likely to be the true ground state of hadronic matter, QSs have been intensively studied (see e.g. [34–38]). Nowadays there is sufficient information about compact objects through the electromagnetic spectrum and gravitational wave detection. Analysis of these observational data has led to constraints on the macroscopic properties such as the mass, radii, and tidal deformability of compact astrophysical objects [1, 9, 39]. Recent data obtained from the Neutron Star Interior Composition Explorer (NICER) led to the detection of two compact objects PSR J0030+0451 and PSR J0740+6620, which further constrain the composition of stellar matter [40–43].

* ai@academico.ufpb.br

† tobias@ita.br

However, these pulsars' exact matter composition is still a research subject. Thus, these observations in recent years have led to robust restrictions on the EoS ruling out most phenomenological quark models. Additionally, it has been established theoretically that, at a high enough baryon density (in the inner core of a compact object) the nucleon Fermi energy is high enough to allow possible new degrees of freedom such as exotic baryons [44–47] and deconfined QM [48, 49]. Since SQM has been conjectured to be the true ground state of QCD [33, 35, 50, 51] it was understood that hadronic matter can transform into QM, transitioning to QSs instead of NSs. As discussed in [52–58], proto-strange QSs with bare or dynamically irrelevant nucleonic matter crust can be formed through BNS merger. That notwithstanding, there is a strong argument against the presence of a crust on QSs [59–61].

In this paper, we employ the DDQM under thermodynamic conditions characteristic of the BNS merger remnant, assuming that the remnant is a NS composed of self-bound free QM. The DDQM is characterized by two free parameters D (a dimensionful constant representing the confining strength) and C (a dimensionless constant representing the deconfinement strength) given through the cubic-root law [62]

$$m_i = m_{i0} + \frac{D}{n_b^{1/3}} + Cn_b^{1/3}, \quad (1)$$

with m_i the equivalent of a dressed quark mass, m_{i0} the current quark mass and n_b the baryon density. The last two terms in (1) can be associated to a Cornell-like potential for confining heavy quarks [63–65], $V_c(r_*) = -\beta/r_* + \sigma r_*$, where σ and β are constants that can be determined through fitting to lattice QCD (lQCD) data. It comprises a Coulomb like term dominant at short distances with strength β from asymptotic freedom and a linear confining part with strength σ , which is also associated with the QCD string tension. In the above expression, the average inter-particle separation distance r_* can be associated with the baryon density through $r_* \sim 1/n_b^{1/3}$. We choose $\sqrt{D} = 127.40$ MeV and $C = 0.8$ reached in [34] through Bayesian analysis of the DDQM at $T = 0$ MeV to serve as a benchmark for our study. These parameters produce a stable QS according to Bodmer and Witten's conjecture which hypothesizes that the binding energy of SQM must be less than the binding energy of ^{56}Fe , i.e. $(\varepsilon/n_b)_{\text{SQM}} \leq 930$ MeV. In the same vein, the two-flavor quark matter (2QM) must satisfy $(\varepsilon/n_b)_{2\text{QM}} > 930$ MeV [33, 35, 66] i.e., the binding energy should be larger for 2QM for u and d quarks to be more tightly bound otherwise, they would dissociate into free u and d quarks. Also, these choices lead to SQS that satisfies the maximum mass constraint of pulsars PSR J0952-0607 [67], PSR J0740+6620 [43] and PSR J0030+0451 [40], and others that satisfy the $2M_\odot$ constraint. We fix the entropy per baryon, S/n_b of the remnant matter, and calculate the temperature profile, particle distributions, speed of sound, polytropic index, and the structure of the star. On the other hand, for

comparison, we consider a remnant matter at a uniform temperature and study the entropy distribution from the disk to the core of the remnant and the other properties of the matter investigated at fixed entropy per baryon.

The paper is organized as follows: In Sec. II, we present the model that serves as the basis for this investigation. This section is divided into four subsections, in Subsec. II A we present the thermodynamic treatment of the model, in Subsec. II B we present the foundation of the mass scaling and its scaling with temperature, in Subsec. II C we present the properties of the SQM under investigation, and finally, we present the thermodynamic conditions for BNS merger in Subsec. II D. We present our findings and analyze them in Sec. III and the final remarks in Sec. IV.

II. THE MODEL

The variation of particle self-energies depending on the media in which they are propagating is well-known in literature [68, 69]. In the simplest case, the mass is usually referred to as the effective mass to distinguish it from the 'bare' mass. When models are expressed in terms of temperature and chemical potentials they are referred to as the quasiparticle models [70] (see e.g. [71–76]).

Now we focus our attention on DDQM, which is used in our study. Indeed, the DDQM is a quasiparticle model originally formulated to investigate the confining characteristics of QM [77, 78] and was later on extended to calculate the EoS [79–82], SQM viscosity and r-modes dissipation [83], diquark properties [84] and compact astrophysical objects [25, 34, 71, 73]. The application of this model to study compact astrophysical objects has largely been successful in fulfilling the $2M_\odot$ mass and radii constraints of NSs, making it a viable QS model. That notwithstanding, it is associated with two known limitations, namely: the equivalent mass scaling and thermodynamic consistency. However, these issues have been tackled by several authors [71, 82, 85, 86] with some promising outcomes.

A. Finite temperature formalism of DDQM

The free energy density of the hot SQM system can be expressed as

$$F = F(T, V, \{n_i\}, \{m_i\}) = \Omega_0(T, V, \{\mu_i^*\}, \{m_i\}) + \sum_{i=u,d,s} \mu_i^* n_i, \quad (2)$$

where μ_i^* is the effective chemical potential for the i th particle, $m_i \rightarrow m_i(n_b, T)$ is the density and temperature dependent particle mass, and Ω_0 is the thermodynamic potential density similar to the non-interacting particle system, which will be used as an intermediate quantity at this point. The thermodynamic potential density Ω will

be determined and presented at the end of this subsection as a function of Ω_0 .

The expression for F has the same form as the well-known expression for the free fermionic system with the particle mass replaced by the equivalent particle mass $m_i(n_b, T)$ and the real chemical potential μ_i replaced by μ_i^* for thermodynamic consistency. We connect μ_i^* and Ω_0 to the independent state variables; T , n_i and the volume V through

$$n_i = -\frac{\partial}{\partial \mu_i^*} \Omega_0(T, V, \{\mu_i^*\}, \{m_i\}), \quad (3)$$

this expression is well-known in thermodynamics with μ_i^* in place of μ_i to ensure thermodynamic consistency. To determine the other thermodynamic quantities, we take a derivative of (3), which yields

$$dF = d\Omega_0 + \sum_i n_i d\mu_i^* + \sum_i \mu_i^* dn_i, \quad (4)$$

here, Ω_0 can be expressed in terms of the dependent variables as

$$d\Omega_0 = \frac{\partial \Omega_0}{\partial T} dT + \sum_i \frac{\partial \Omega_0}{\partial \mu_i^*} d\mu_i^* + \sum_i \frac{\partial \Omega_0}{\partial m_i} dm_i + \frac{\partial \Omega_0}{\partial V} dV, \quad (5)$$

and the equivalent mass as

$$dm_i = \frac{\partial m_i}{\partial T} dT + \sum_j \frac{\partial m_i}{\partial n_j} dn_j. \quad (6)$$

Combining (4), (5) and (6) and regrouping terms, we find that:

$$dF = \left(\frac{\partial \Omega_0}{\partial T} + \sum_i \frac{\partial \Omega_0}{\partial m_i} \frac{\partial m_i}{\partial T} \right) dT + \sum_i \left(\mu_i^* + \sum_j \frac{\partial \Omega_0}{\partial m_j} \frac{\partial m_j}{\partial n_i} \right) dn_i + \frac{\partial \Omega_0}{\partial V} dV. \quad (7)$$

Comparing the above result to the standard expression for the thermodynamic free energy density;

$$dF = -SdT + \sum_i \mu_i dn_i + \left(-P - F + \sum_i \mu_i n_i \right) \frac{dV}{V}, \quad (8)$$

where S is the entropy density and P is the pressure of the system, we identify:

$$S = -\frac{\partial \Omega_0}{\partial T} - \sum_i \frac{\partial m_i}{\partial T} \frac{\partial \Omega_0}{\partial m_i}, \quad (9)$$

and

$$P = -F + \sum_i \mu_i n_i - V \frac{\partial \Omega_0}{\partial V}, \quad (10)$$

where the real chemical potential is given in terms of the effective one as

$$\mu_i = \mu_i^* + \sum_j \frac{\partial \Omega_0}{\partial m_j} \frac{\partial m_j}{\partial n_i} \equiv \mu_i^* - \mu_I, \quad (11)$$

where μ_I is the chemical potential that carries the interaction. For an infinitely large system of SQM, Eq. (2) is independent of the volume of the system and hence (10) takes the form:

$$P = -F + \sum_i \mu_i n_i = -\Omega_0 + \sum_{i,j} n_i \frac{\partial \Omega_0}{\partial m_j} \frac{\partial m_j}{\partial n_i}, \quad (12)$$

in the second step we have substituted (2) in place of F and (11) in place of μ_i to obtain a result in terms of Ω_0 and μ_i^* . Similar expressions were derived in [72, 85, 87] for DDQM using a thermodynamic consistent approach, and in [82] using the general ensemble theory. Additionally, the last term in (10) only persists if the finite size effect of the system cannot be overlooked whether the particle masses are fixed or not. The energy density of the system can then be determined from the fundamental relation with the Helmholtz free energy, namely $\varepsilon = F - TS$, by substituting (2) and (9), resulting in:

$$\varepsilon = \Omega_0 + \sum_i \mu_i^* n_i - T \frac{\partial \Omega_0}{\partial T} - T \sum_i \frac{\partial m_i}{\partial T} \frac{\partial \Omega_0}{\partial m_i}. \quad (13)$$

Finally, the real thermodynamic potential density Ω of the system can be determined as

$$\Omega = F - \sum_i \mu_i n_i = \Omega_0 - \sum_{i,j} n_i \frac{\partial \Omega_0}{\partial m_j} \frac{\partial m_j}{\partial n_i}. \quad (14)$$

It should be noted that the Ω_0 is composed of both particle and anti-particle, therefore, the full contribution will be $\Omega_0^\pm = \Omega_0^- + \Omega_0^+$ with Ω_0^- and Ω_0^+ representing particle and antiparticle contributions respectively. Consequently, the explicit expression for the Ω_0^\pm is given as

$$\Omega_0^\pm = - \sum_i \frac{g_i T}{2\pi^2} \int p^2 dp \left[\ln[1 + e^{-(\epsilon_i - \mu_i^*)/T}] + \ln[1 + e^{-(\epsilon_i + \mu_i^*)/T}] \right], \quad (15)$$

where $i = u, d, s, e, \mu, \nu_\mu$ and ν_e represents the quarks and leptons present in the system and g_i the degeneracy factor. The number density of each fermion species is also given by two terms, $n_i^\pm = n_i^+ - n_i^-$ thus,

$$n_i^\pm = -\frac{\partial \Omega_0^\pm}{\partial \mu_i^*} = \sum_i \frac{g_i}{2\pi^2} \int_0^\infty p^2 dp \left[\frac{1}{1 + e^{(\epsilon_i - \mu_i^*)/T}} - \frac{1}{1 + e^{(\epsilon_i + \mu_i^*)/T}} \right]. \quad (16)$$

The derivatives in S , μ_i^* , P , and, ε can be written explicitly as

$$\frac{\partial \Omega_0^\pm}{\partial m_i} = \sum_i \frac{g_i m_i}{2\pi^2} \int_0^\infty \left[\frac{1}{e^{(\varepsilon_i - \mu_i^*)/T} + 1} + \frac{1}{e^{(\varepsilon_i + \mu_i^*)/T} + 1} \right] \frac{p^2 dp}{\varepsilon_i}, \quad (17)$$

and

$$\begin{aligned} \frac{\partial \Omega_0^\pm}{\partial T} &= -\frac{g_i}{2\pi^2} \int_0^\infty \left(\ln \left[1 + e^{-(\varepsilon_i - \mu_i^*)/T} \right] \right. \\ &\quad + \frac{(\varepsilon_i - \mu_i^*)/T}{1 + e^{-(\varepsilon_i - \mu_i^*)/T}} + \ln \left[1 + e^{-(\varepsilon_i + \mu_i^*)/T} \right] \\ &\quad \left. + \frac{(\varepsilon_i + \mu_i^*)/T}{1 + e^{-(\varepsilon_i + \mu_i^*)/T}} \right) p^2 dp, \end{aligned} \quad (18)$$

with $\varepsilon_i = \sqrt{p^2 + m_i^2}$.

B. Mass scaling with temperature

We will adopt the cubic-root equivalent mass scaling formula originally derived for $T = 0$ [62, 87] and was extended for a finite temperature treatment [72, 85]. The derivation of quark mass scaling and its thermodynamic consistency have been elaborated in [62, 72]. We do not intend to repeat the derivation here, but we will highlight the parts fundamental to this work and focus more on how we intend to introduce temperature into the system. We start with the QCD Hamiltonian density

$$H_{\text{QCD}} = H_k + \sum_{q=u, d, s} m_{i0} \bar{q}q + H_I, \quad (19)$$

with H_k the kinetic term and H_I the interaction term. We now introduce an equivalent Hamiltonian density with the interacting term absorbed into an equivalent mass m_i in the form

$$H_{\text{eqv}} = H_k + \sum_{q=u, d, s} m_i \bar{q}q, \quad (20)$$

hence,

$$m_i = m_{0i} + m_I, \quad (21)$$

this means to keep the energy of the system of free quarks constant, its mass must be m_i . To determine m_i , we impose the condition that H_{eqv} and H_{QCD} must have the same eigenvalues for the same eigenstates, $|n_b, T\rangle$ i.e.,

$$\langle n_b, T | H_{\text{QCD}} | n_b, T \rangle = \langle n_b, T | H_{\text{eqv}} | n_b, T \rangle, \quad (22)$$

applying the same equality to the vacuum state $|0\rangle$ and taking the difference we obtain

$$m_i = m_{i0} + \frac{\langle H_I \rangle_{n_b, T} - \langle H_I \rangle_0}{\sum_q \left[\langle \bar{q}q \rangle_{n_b, T} - \langle \bar{q}q \rangle_0 \right]}, \quad (23)$$

therefore m_I can be identified with,

$$m_I = \frac{\langle H_I \rangle_{n_b, T} - \langle H_I \rangle_0}{\sum_q \left[\langle \bar{q}q \rangle_{n_b, T} - \langle \bar{q}q \rangle_0 \right]}. \quad (24)$$

We remark that the interacting part of the equivalent quark mass, m_I , depends on the interaction energy density, and the relative quark condensates (the denominator of the above expression) which are assumed to be flavor independent. For color confinement and asymptotic freedom, m_I must satisfy

$$\lim_{n_b \rightarrow 0} m_I \rightarrow \infty; \quad \text{color confinement condition} \quad (25)$$

and

$$\lim_{n_b \rightarrow \infty} m_I \rightarrow 0; \quad \text{asymptotic freedom condition.} \quad (26)$$

The proposed structure of the equivalent mass in terms of n_b is

$$m_i = m_{i0} + \frac{D}{n_b^z}, \quad (27)$$

consequently, $z > 0$ satisfies the conditions (25) and (26). Assuming the quarks are confined, the interaction energy density depends on the particle density, while the linear confining potential, $V_c(r_*, T)$, is a function of the average inter-particle separation distance r_* and T . Explicitly,

$$\langle H_I \rangle_{n_b, T} - \langle H_I \rangle_0 = 3n_b V_c(r_*, T), \quad (28)$$

where factor 3 is due to the number of quark flavors participating in the strong interaction. The average quark-quark distance is related to n_b by

$$r_* \sim \frac{1}{n_b^{1/3}}, \quad (29)$$

we have adopted the cubic-root law where z was determined to be 1/3 in [62, 72, 87]. The confining potential is well-known in LQCD to be proportional to r_* in the form $V_c(r_*, T) = \sigma(T)r_*$, where σ is the proportionality constant known as the string tension [88–90], with this expression, (26) and (25) are satisfied;

$$\lim_{n_b \rightarrow \infty} V_c(r_*, T) \rightarrow 0, \quad (30)$$

which expresses the asymptotic freedom and, on the other hand, the low-density limit:

$$\lim_{n_b \rightarrow 0} V_c(r_*, T) \rightarrow \infty, \quad (31)$$

represents color confinement.

The potential V_c has been widely investigated as a function of temperature in the literature – see, for example, Refs. [91–93] –, it was found in all cases that the string tension decreases with temperature and vanishes at $T = T_C$ (T_C is the critical temperature) i.e.,

$\sigma(T = T_C) = 0$. Hence, the normalized $\sigma(T)$ can generally be expressed as

$$\frac{\sigma(T)}{\sigma_0} = \left[1 - \frac{T^2}{T_C^2}\right]^\gamma, \quad (32)$$

where γ is a constant usually determined in the model framework and σ_0 is the string tension determined at $T = 0$. We adopt the case in which $\gamma = 1$ as applied in [94] to a density and temperature-dependent quark mass in the framework of the MIT bag model. Also, a phenomenological study of quark and glueball confinements in [95] arrived at a similar outcome. The denominator of (24) is compared to the chiral condensate in the QCD vacuum in a simplified form. Even though the general expression must include density and temperature dependence, for simplicity without loss of generality, we will consider only density-dependent and use the well-known model-independent quark condensate in nuclear matter [96, 97],

$$\frac{\langle \bar{q}q \rangle_{n_b}}{\langle \bar{q}q \rangle_0} = 1 - \frac{n_b}{n_b^*}, \quad (33)$$

where n_b^* is related to the pion mass M_π , the pion decay constant f_π , and the pion-nucleon sigma term σ_N in a form,

$$n_b^* = \frac{M_\pi^2 f_\pi^2}{\sigma_N}. \quad (34)$$

Substituting (28) and (33) into (24) and rescaling D as

$$D \sim -\frac{3\sigma_0 n_b^*}{\sum_q \langle \bar{q}q \rangle_0}, \quad (35)$$

we get

$$m_I = \frac{D}{n_b^{1/3}} \left[1 - \frac{T^2}{T_C^2}\right]. \quad (36)$$

therefore, the full expression in (23) becomes

$$m_i = m_{i0} + \frac{D}{n_b^{1/3}} \left[1 - \frac{T^2}{T_C^2}\right], \quad (37)$$

in this expression, the interacting part vanishes when $T = T_C$, similar to the QCD string-breaking scenario however, the current quark mass permanently breaks the chiral symmetry.

Comparing the above expression to the well-known Cornell potential $V(r_*) = -\beta/r_* + \sigma r_*$, which incorporates both the confinement and the asymptotically free behavior of the QM, one can introduce a deconfinement parameter proportional to n_b , looking at the Coulomb part of the Cornell potential, thus, $z < 0$ in (27). The Cornell potential has been widely explored in phenomenological and lQCD and it has been proven to show characteristics consistent with the behavior of QCD

matter. This additional term is necessary to balance the attractive pressure generated by the linear confining term to support the star to attain the maximum required mass for NSs without collapsing. In this case, the full expression becomes

$$m_i = m_{i0} + \frac{D}{n_b^{1/3}} \left[1 - \frac{T^2}{T_C^2}\right] + C n_b^{1/3} \left[1 - \frac{T^2}{T_C^2}\right]^{-1}. \quad (38)$$

From (1) the confining strength is represented by D and the Coulomb-like strength is represented by C and their values can be determined through stability analysis. In quenched lQCD the T_C is determined to be around $T_C \sim 270$ MeV [98–101].

C. Properties of the SQM

The SQM is, as usual, composed of up (u), down (d), and strange (s) quarks with leptons (electrons e and muons μ with their corresponding neutrinos ν_e and ν_μ respectively) in β -equilibrium. Due to the weak interactions, such as $d, s \leftrightarrow u + e + \bar{\nu}_e$, $s + u \leftrightarrow u + d$, etc., the β -equilibrated matter are required to satisfy the chemical equilibrium condition,

$$\mu_d^* = \mu_s^* = \mu_u^* + \mu_l - \mu_{\nu_l}, \quad (39)$$

where the subscripts represent the particles present, $\mu_l = \{\mu_e, \mu_\mu\}$ and $\mu_{\nu_l} = \{\mu_{\nu_e}, \mu_{\nu_\mu}\}$. It is important to mention here that the real chemical potentials μ_i satisfy the same chemical equilibrium relation as the effective ones above (see Ref.[71]). Charge neutrality of the system requires that

$$\frac{2}{3}n_\mu - \frac{1}{3}n_d - \frac{1}{3}n_s - n_e - n_\mu = 0, \quad (40)$$

here, n_i is the particle number density and the subscript i represents the identity of the particle present. The baryon number is also conserved through

$$n_b = \frac{1}{3}(n_u + n_d + n_s) = \frac{1}{3} \sum_i n_i. \quad (41)$$

At finite temperature where neutrinos are trapped in the SQM, we fix separately, the lepton numbers; $Y_{L,e} = Y_e + Y_{\nu_e}$ and $Y_{L,\mu} = Y_\mu + Y_{\nu_\mu}$, with $Y_{L,e} = (n_e + n_{\nu_e})/n_b$ and $Y_{L,\mu} = (n_\mu + n_{\nu_\mu})/n_b$ for electron and muon families respectively. The thermodynamic conditions are based on the astrophysical phenomena under consideration. It is known that neutrinos are trapped in the stellar matter when their mean-free path is less than the size of the system (typically the radius of the stellar object) [102, 103]. Also, the electron and muon neutrino spheres are not identical hence, the trapping regime might be related to a family of leptons. Therefore we fix the lepton numbers separately for each family of leptons and ignore the τ leptons, assuming they are too heavy to be relevant.

The quark flavors have degeneracy of $g_i = 6$ (3 colors \times 2 spins), the e , the μ have a degeneracy of $g_i = 2$ and the neutrinos have degeneracy of $g_i = 1$. The current quark masses for u , d , and s used are 2.16 MeV, 4.67 MeV, and 93.4 MeV respectively as reported in the PDG [104]. We choose a critical temperature, $T_C = 270$ MeV, the strength of the linear confinement, $\sqrt{D} = 127.40$ MeV, and the dimensionless single gluon-exchange interaction strength, $C = 0.8$. The values of C and D were taken from [34] determined at $T = 0$ using Bayesian study and stability analysis to serve as a benchmark for our analysis. The EoS and the other remnant properties were determined by either fixing T and calculating S/n_b or fixing S/n_b and calculating the temperature profile in addition to the other properties.

D. Thermodynamic conditions for the BNS merger remnants

The thermodynamic conditions such as the lepton number concentration, entropy per baryon, and temperature were derived from BNS simulations results [2, 12, 105–107]. The degrees of freedom considered in BNS merger simulations are nucleons, nuclei, electrons, and positrons. Aside from that, some include hyperons, quarks, and/or neutrinos [20, 108–111]. On the other hand, most state-of-the-art simulations of binary NS mergers do not include muons, even though the exotic temperature and density conditions in the BNS merger event favor their generation. A recent simulation of BNS postmerger remnants [112] considering muons shows that their presence significantly affects the EoS. In this work, we include muons and their neutrinos in our numerical codes to study their effect on the EoS, particularly, we pay attention to the production of ν_e and ν_μ as the merger remnant evolves, assuming it does not form a black hole promptly.

Muons are known to play a vital role in the microphysics of cold NSs and are expected to be significant in mergers where the thermodynamic conditions rather favor their production. The two NSs that participated in the merger event were originally in a quasi-circular orbit until the emission of GWs caused their merger – see a review on this subject in [2]. In the merging process, the two stars are compressed a few times n_0 ($n_0 = 0.152 \text{ fm}^{-3}$ is the nuclear saturation density [113]) and heated substantially resulting in supersonic velocities and shock wave formation. This provokes a sharp rise in temperature and local entropy production. Considering that the BNS merger ejecta comes from the crust and the outer core of two NSs, the initial lepton number is expected to be low. It should be noted that cold NSs are associated with low lepton fractions. The stellar matter of the two cold NSs have lepton fractions in the range of $0.00 \leq Y_{L,l} \leq 0.2$ [23, 114]. We chose $Y_{L,e} = Y_{L,\mu} = 0.1$ as the working assumption for our analysis similar to the study of a merger event in hadronic stars in [103, 115].

The cores of the NSs are not significantly shocked at

merger so, the entropy per baryon of the remnant core is estimated to be $S/n_b \lesssim 2k_B$ (k_B is the Boltzmann constant), here, we chose $S/n_b = 1k_B$ for our analysis. When there is a prompt black hole (BH) formation, the apparent horizon removes the high-density part leaving a relatively cold disk with a slightly higher lepton fraction, $Y_{L,e} = Y_{L,\mu} = 0.25$. At this point, the entropy of the remnant also increases and the evolution process terminates here, therefore, we chose $S/n_b = 1.5k_B$ for our analysis. When the action of the inspiral arms on the innermost part of the disk increases the entropy of the remnant and the temperature also increases accordingly. The estimated entropy at this stage is around $2 < S/n_b[k_B] \lesssim 10$ however, we chose a lower limit of $S/n_b = 3k_B$ and an upper limit of $S/n_b = 6k_B$ for our analysis. In [116] the authors used the thermodynamic conditions of BNS merger and heavy ion collision to probe their similarities and differences. In this study, the entropy flow from these two events played a key role. Additionally, we considered the QM at uniform temperature with a lower limit of $T = 5$ MeV (neutrino trapping temperature) and an upper limit of $T = 50$ MeV to study the S/n_b variation with n_b . Although there is a wide spread of T and S/n_b at the initial stages of the remnant’s evolution, these thermodynamic conditions become homogeneous in the remnant matter at the latter stages of its evolution.

Moreover, matter under extreme conditions of temperature and densities above the n_0 are also formed through core-collapse supernovae (CCSN) explosions, aside from the BNS merger remnant, leading to the formation of PNSs that go through several evolution stages to form an NS or a BH. The difference between the CCSN remnant and BNS merger remnant is that, the latter involves a higher isospin asymmetry due to excess neutron over protons in NS-NS or NS-BH merger events (see [107] for a review). In the case of CCSN the core of the massive star traps neutrinos (particularly ν_e) which heats it, and expands it before the explosion occurs. This process increases the proton fraction at the initial stage of the star’s birth before deleptonization sets in after the core bounce causing a reduction in the proton fraction in the PNS as it cools down to a cold NS [29, 117]. In the case of a BNS merger, the proton fraction in the two cold NSs that initially take part in the merger is small. There has been an enormous effort in the past few years in theory, laboratory experiments, and astrophysical observations to constrain the thermodynamic properties and the chemical composition of stellar matter under the conditions of CCSN and NS mergers. This is necessary because of the link between the macroscopic remnant structure during the evolution of such stellar remnants and the fundamental interactions between their constituents at the microscopic level. These motivate the study of such objects since they contribute to the effort in creating general-purpose EoSs and also challenge our understanding of nature on both scales.

III. RESULTS AND ANALYSIS

In Table I we show the lepton fraction $Y_{L,l}$, the maximum mass M_{\max} , its radii R , entropy per baryon S/n_b , core temperature T_c , and the central energy and baryon densities, ε_0 and n , respectively. We observe that the M_{\max} and R increase by increasing S/n_b , while ε_0 and n decrease causing a rise in the core temperature of the NS remnant matter. In the case of an increase in $Y_{L,l}$ and S/n_b (condition for prompt formation of a black hole) the M_{\max} , R and T_c increases with a decrease in ε_0 and n_0 . For uniform temperature matter, a hotter QM has higher M_{\max} and R while ε_0 and n_0 decrease, as usual. Naturally, the ratio ε_0/n increases as S/n_B rises and T increases. It has been established (see [6, 12]) that a typical density in BNS merger remnant is between $2n_0$ and $6n_0$, this agrees with the values of n on Table I which ranges between $2.7n_0$ and $4n_0$. Following the tabulated results for fixed S/n_b and T , hotter remnants accrete more mass and increase in size.

In Fig. 1, we show the particle distributions, assuming that the NS remnant has a uniform temperature using the relation

$$Y_i = \frac{n_i}{n_u + n_d + n_s}, \quad (42)$$

where i represents the individual particles present. Comparing the particle distributions in the upper panels, we observe that at low T we have a higher d -population relative to u and delayed appearance of the s -quark at low n_b regions. The e 's and μ 's show a marginal increase in the hotter remnant matter. In both cases, the particles do not show any significant changes at higher densities beyond $n_b \sim 2.5n_0$. Also, higher T produces more ν_e population while ν_μ only increases marginally at higher n_b and rather shows a decrease at low n_b with an early appearance of the s -quark and μ in the remnant matter.

These effects at higher T causes an increase in the M_{\max} and R as can be seen on Table I. The isospin asymmetry (or $u - d$ quark asymmetry),

$$\delta = 3 \frac{n_d - n_u}{n_d + n_u}, \quad (43)$$

with $n_3 = n_d - n_u$, the isospin density and $n_b = (n_d + n_u)/3$ the baryon density for two flavor quark systems. The δ is higher in the low T remnant matter due to excess of d -quark relative to u at densities below $n_b \sim 2.7n_0$. In the lower panel, we show the S/n_b contribution of each particle to the overall S/n_b . We observe that temperature increase significantly increases the entropy of the particles, as expected, from low n_b/n_0 and steadily falls towards the center of the remnant. The d -quark shows a higher S/n_b contribution while ν_e shows the least contribution in both cases.

In Fig. 2, we show the net S/n_b as a function of n_b/n_0 . We observe a higher S/n_b in hotter QM, as expected. The S/n_b is higher towards the surface (low n_b) of the remnant matter where the disk is formed and decreases

toward the center (high n_b). The BNS merger is associated with net angular momentum and is gravitationally bound, however, thermodynamics in the local rest frame of the system remains relevant. In the absence of physical viscosity, the matter flow is isentropic, hence S/n_b can serve as a meaningful tool for analysis. It has been found in [118] that entropy rise is associated with neutrino absorption with an initial value in the disk estimated at $S/n_b \sim 5 - 10k_B$ and rise to $S/n_b \sim 15 - 20k_B$ in the later stages of the remnant evolution. We can deduce that, in the model framework, the ν_e contributes highly to the rise in the entropy compared to the ν_μ . The muon neutrinos have higher chemical potentials compared to the electrons, this means the Ω_0 becomes more negative and S becomes more positive for the same T , see Eqs. (9) and (15) together.

In Fig. 3, we show four snapshots of the evolution stages of the postmerger NS remnant. The first stage (top left) is the Y_i in the core of the remnant at the merger, $t \sim 0$. At this stage, the innermost part of the merging NS cores $n_b > n_0$ does not experience significant shocks so the S/n_b in the central part of the remnant remains low, it is estimated to be around $1 \lesssim S/n_b[k_B] \lesssim 2$. This stage is characterized by a small temperature profile in the core, mainly generated by matter compression of degenerate nuclear matter above n_0 . At this stage, we use the initial conditions $S/n_b = 1$ and $Y_{L,l} = Y_{L,e} = Y_{L,\mu} = 0.1$ for the analysis, because at $t \sim 0$, the lepton fractions in the cores of the two NSs is frozen to the initial neutrino-less (ν -less) cold weak equilibrium value, which is estimated to be in the range $0.0 \lesssim Y_{L,l} \lesssim 0.2$ (this estimate was initially made for only electrons but we generalize it to include muons) towards the higher baryon density regions. The second panel (top right) is based on the assumption of prompt formation of a black hole. In this case, the thermodynamic conditions change drastically. The formation of an apparent horizon removes all the high-density part of the remnants leaving a cold disk with an estimated temperature of about $T \lesssim 10$ MeV, with a significant reprocessed lepton fraction of about $Y_{L,l} \sim 0.25$. At this stage the disk entropy is slightly higher than when massive NS is present at the center, hence, we used $S/n_b = 1.5k_B$ as our working assumption. Comparing the Y_i in the two panels we can see that the Y_i in the right panel has less isospin asymmetry due to excess u -quark relative to d . Also, there is more e , μ , ν_μ and ν_e content due to higher $Y_{L,l}$. At some dynamical timescales, a few milliseconds after the merger, if the remnant does not form a black hole promptly, the inspiral arms' activities at the disk's central part increase the entropy of the remnant matter, creating a strong correlation between the matter density and entropy. The highest temperature of the stream is expected at this stage, however, they may rapidly decrease because of fluid expansion and neutrino diffusion. The lepton fraction is reset to the initial condition due to excess lepton antineutrino emissions and absorption. The entropy at this stage is also estimated to be between $2 \leq S/n_b[k_B] \lesssim 10$. In the

$S/n_B [k_B]; Y_{L,l}$	$M_{max} [M_\odot]$	$R [\text{km}]$	$\varepsilon_0 [MeV fm^{-3}]$	$n [fm^{-3}]$	$T_c [MeV]$
1; $Y_{L,e} = Y_{L,\mu} = 0.1$	2.25	14.30	685	0.59	9.02
1.5; $Y_{L,e} = Y_{L,\mu} = 0.25$	2.34	14.78	635	0.52	12.17
3; $Y_{L,e} = Y_{L,\mu} = 0.1$	2.33	14.69	634	0.54	26.71
6; $Y_{L,e} = Y_{L,\mu} = 0.1$	2.67	16.45	498	0.41	51.30
T = 5; $Y_{L,e} = Y_{L,\mu} = 0.1$	2.25	14.36	662	0.59	—
T = 50; $Y_{L,e} = Y_{L,\mu} = 0.1$	2.57	16.92	483	0.41	—

TABLE I. BNS remnant properties.

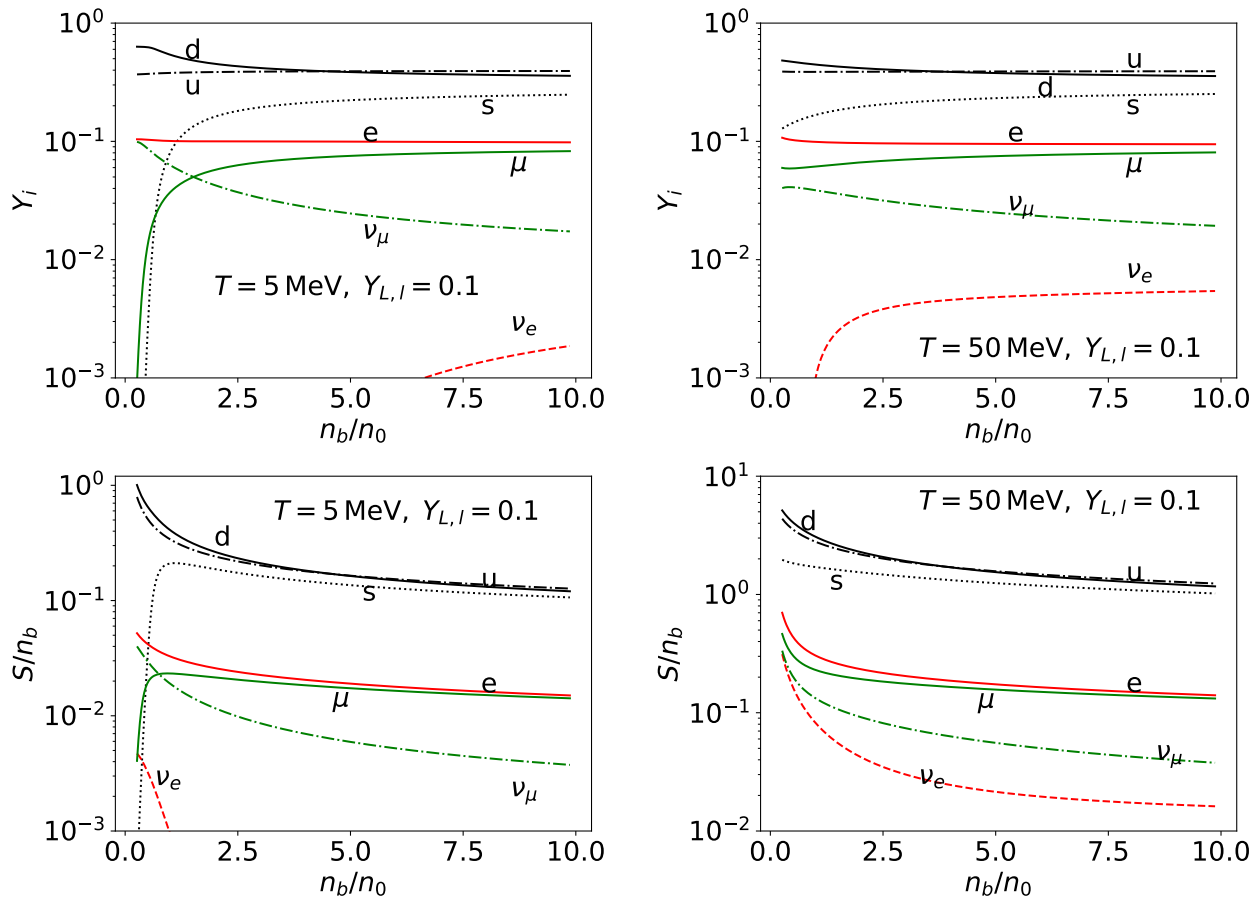


FIG. 1. In this diagram we show the Y_i as a function of n_b/n_0 . In the upper panel, we choose two values of T ; a lower limit of $T = 5$ MeV at which neutrinos are trapped in the remnant matter, and an upper limit $T = 50$ MeV, using $Y_{L,e} = Y_{L,\mu} = 0.1$ and their corresponding S/n_b distribution for each particle in the bottom panel.

bottom panels, we set lower and upper limits for S/n_b to study the particle distribution as the S/n_b increases through the evolution of the merger remnant. Comparing the first panel (bottom left) and the second panel (bottom right) we observe that the NS remnant absorbs more neutrinos as the S/n_b increases, particularly the ν_e is significantly enhanced while ν_μ only increases marginally. The isospin asymmetry also decreases as S/n_b increases. Comparing the Y_i for the initial condition at merger (top right panel) and the two panels below following the evolution of the NS remnant, assuming it did not form a

black hole promptly, the fraction of ν_e significantly increases and the isospin asymmetry decreases along the evolution lines. It is worth pointing out that, through the evolution stages, only a fraction of ν_e show significant variation at all densities as the NS remnant evolves. Additionally, higher S/n_b facilitates the emergence of μ and s -quarks but their effects can be seen at relatively low n_b and does not show any significant variation along the evolution stages at $n_b \approx 1.6n_0$ and above.

Fig. 4 shows the EoS of both the fixed entropy NS remnants and the uniform temperature ones. We observe

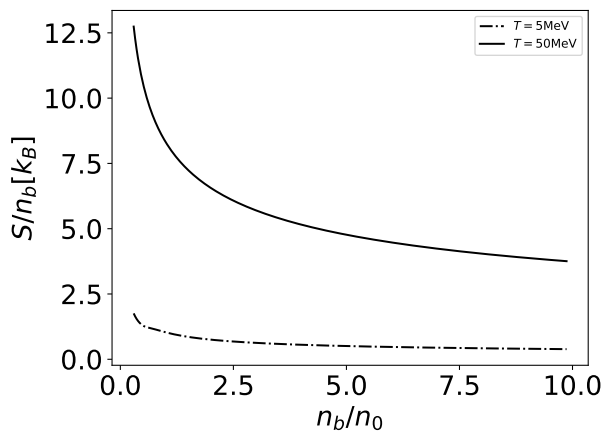


FIG. 2. Net entropy of the particles per baryon at different fixed temperatures as a function of baryon density. Solid line for $T = 50$ MeV and dot-dashed line for $T = 5$ MeV.

that, in the case of $T = 50$ MeV, the EoS is stiffer at low ε and begins to soften at the higher ε compared to the $S/n_b = 6k_B$ case. This effect can be associated with the increase of the strength of the term proportional to $n_b^{1/3}$ in the equivalent quark mass as T increases. Comparing the maximum masses and radii data on Table I, we observe that the fixed entropy NS remnant is more compact than the uniform temperature one. Also, comparing their neutrino content, Figs. 1 (top panel, right) and 3 (bottom panel, right), we can see that the $S/n_b = 6k_B$ remnant has visibly high ν_e content, particularly towards the center of the NS remnant.

Interestingly, as we see in Fig. 4, the initial conditions for uniformly heated remnant matter at $T = 5$ MeV coincides with the initial condition set for the fixed entropy remnant matter, even though it has a relatively higher core temperature of $T_c \sim 9$ MeV. Their EoSs exactly overlap each other with no distinguishable differences. Comparing their particle fractions, Figs. 1 (top panel, left) and 3 (top panel, left), they have almost the same ν_e content and early appearance of the s -quark and μ , their δ are also comparably the same. Generally, hotter remnant matter has stiffer EoS than their relatively colder counterparts, similarly, higher S/n_b remnant matter has stiffer EoS than relatively lower S/n_b ones since higher values of S/n_b means higher T . In the case of $S/n_b = 1.5k_B$ an increase in the $Y_{L,l}$ stiffens the EoS as well. We can deduce from the particle distribution in the NS remnant matter that a delayed appearance of μ , ν_e and s -quark rather softens the EoS and leads to lower maximum masses and radii. Likewise, a higher ν_e content in the NS remnant matter leads to a stiffer EoS. Moreover, stiffer EoS are associated with low central energy and baryon densities as shown on Table I.

In Fig. 5, we show the temperature variations in the NS remnant matter as a function of n_b/n_0 . At the contact interface of the two NSs, matter from their crust and the outer cores slips out and mix causing instability.

The cores originally behind these contact interfaces begin to fuse over time, at this point, a series of compressions and expansions occur while the remnants bounce severally. Hence, temperature and density increase immediately after the merger due to these compressions, oscillations and bounce dynamics [12, 119]. Besides, the high sound velocity of the nuclear matter ($c_s \gtrsim 0.2c$) and nuclear supra-densities ($n_b \gtrsim n_0$) prevent the generation of hydrodynamics shocks in the cores of the two coalescing NSs, thus, the temperature remains low (estimated to be $T \gtrsim 10$ MeV) in the core at merger.

In Fig. 5, we observe that the temperature profile is at its least at the initial merging phase when $S/n_b = 1$ ($T_c \sim 9$ MeV) compared to the other stages when S/n_b was higher (temperature profile for $t \sim 5$ ms postmerger has been studied in [106] as a function of n_b). When the remnant promptly forms a black hole, the S/n_b increases, and the maximum density decreases, as can be seen in Fig 3 for $S/n_b = 1.5k_B$, which corresponds to a higher temperature ($T_c \sim 12$ MeV) and lower central density relative to the first stage. The evolution process terminates when the remnant forms a black hole promptly. Furthermore, when the remnant continues evolving as an NS, the cores of the coalescing NSs continue to fuse, causing compression and shear dissipation, increasing the entropy and as a result, the temperature. We choose a lower limit of $S/n_b = 3k_B$ and an upper limit of $S/n_b = 6k_B$ to obtain a fair idea of the temperature variations at this stage of the remnant evolution, we found $T_c \sim 27$ MeV and $T_c \sim 51$ MeV respectively (higher temperatures in the range of $T \sim 70 - 110$ MeV were determined in [119] and $T \sim 158$ MeV reported in [112]). Comparing Figs. 5 and 3 we can deduce that higher S/n_b are associated with higher ν_e production and an early appearance of μ and s -quark in the remnant matter.

In Fig. 6, we determine the structure of the NS remnant by calculating the mass-radius (M-R) diagram using the Tolman–Oppenheimer–Volkoff equation (TOV) [120] given by the expressions

$$\frac{dP(r)}{dr} = -[\varepsilon(r) + P(r)] \frac{M(r) + 4\pi r^3 P(r)}{r^2 - 2M(r)r}, \quad (44)$$

$$\frac{dM(r)}{dr} = 4\pi r^2 \varepsilon(r), \quad (45)$$

with r the radial coordinate, $M(r)$ the gravitational mass, $P(r)$ the pressure, and $\varepsilon(r)$ the energy density, here, we use the natural units ($G = \hbar = c = 1$). The initial condition is two equal-mass NSs with a combined mass estimated to be $2.74_{-0.01}^{+0.04} M_\odot$ and individual masses between 1.17 and 1.6 M_\odot [1, 40, 121], neglecting the effect of spin in the analysis based on the assumption that most systems are practically not rotational at merger [122]. Generally, NSs have a known mass threshold of about $2M_\odot$ [41, 42] whereas stellar black hole masses observed in binaries are greater than the GW170817 components [123, 124]. We compare our results with the measured mass and radii of the millisecond pulsar PSR J0740+6620 determined through the observation

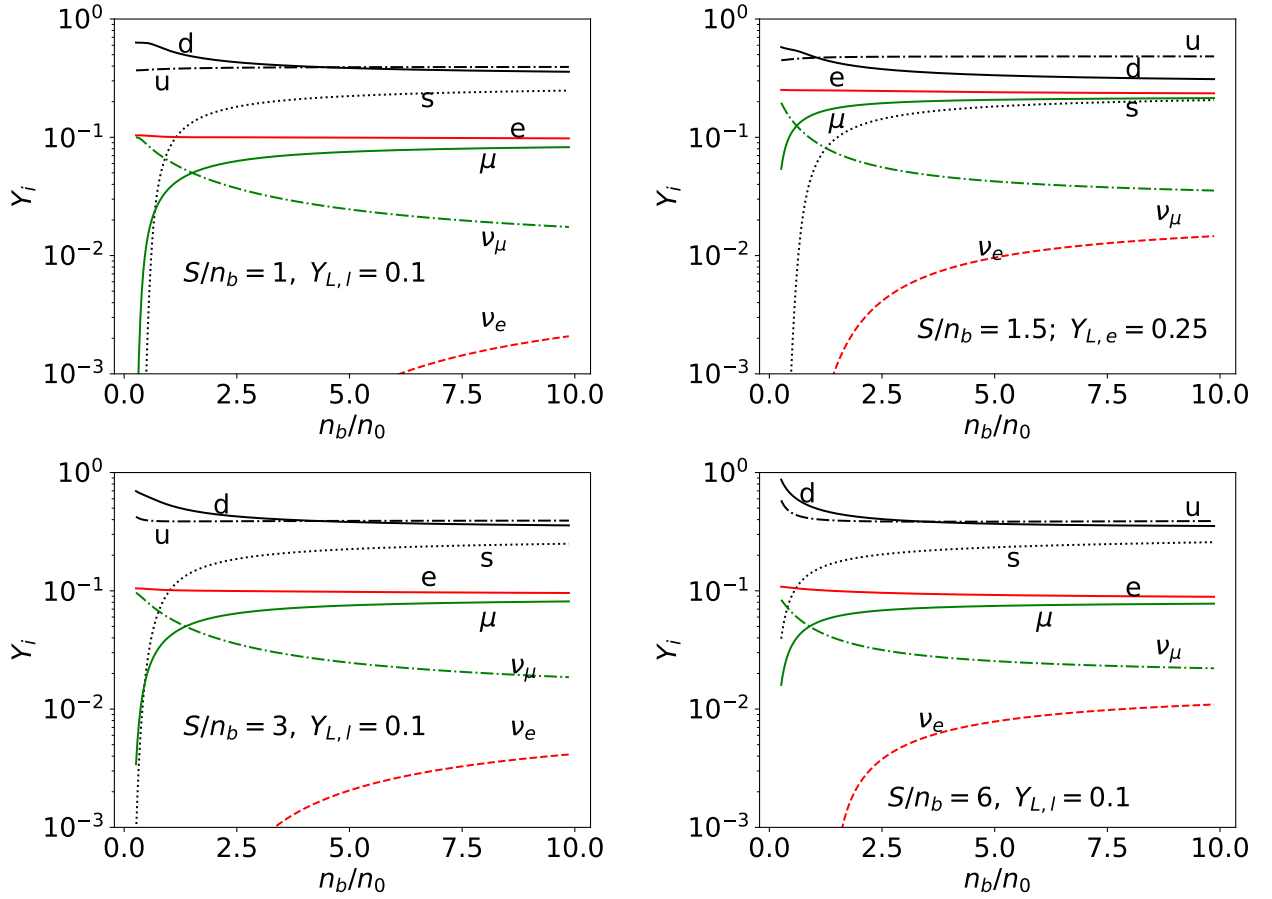


FIG. 3. We show the Y_i for fixed entropy BNS remnants. The first panel (top left) shows the initial condition at merger $t \sim 0$ (t is time), and the second panel (top right) shows the Y_i in the remnant disk assuming there was prompt collapse of the remnants to a black hole. The bottom panels show two stages after the merger $t > 0$.

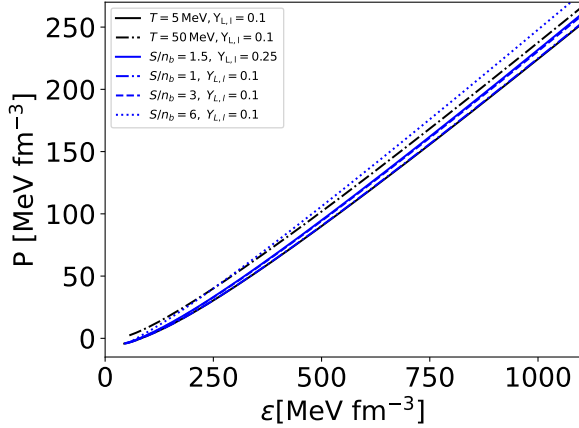


FIG. 4. The EoSs for hot quark matter.

and analyses of the NICER X-ray observatory data. The estimated measured masses and radii were $2.07^{+0.07}_{-0.07}M_{\odot}$ and $2.08^{+0.09}_{-0.09}M_{\odot}$ at 68% confidence level (CL); and radii $12.39^{+1.30}_{-0.98}$ km [43] and $13.71^{+2.61}_{-1.50}$ km [125] determined by

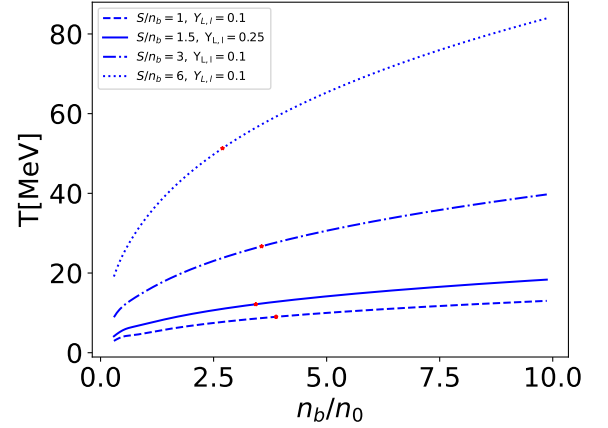


FIG. 5. The temperature profiles of the fixed entropy NS remnant matter as a function of the n_b . The red stars in the curves represent the position of the core temperature.

different groups. It is worth mentioning that the mass of this pulsar was also independently determined to be $2.08^{+0.07}_{-0.07}M_{\odot}$ through Shapiro delay effect [41]. The mass

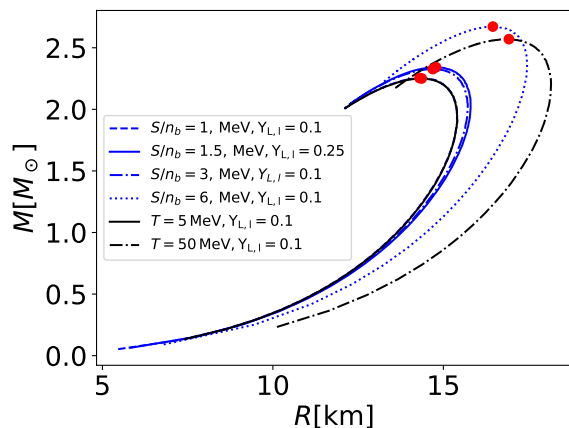


FIG. 6. The mass-radius diagram of hot NS remnant. The red dots represent the precise point of the maximum mass and radii of the remnant star.

and radii of PSR J0030+0451 determined through fitting to the NICER data led to two predictions (at 68% CL); $M = 1.34^{+0.15}_{-0.16} M_{\odot}$, $R = 12.71^{+1.14}_{-1.19}$ km [40] and $M = 1.44^{+0.15}_{-0.14} M_{\odot}$, $R = 13.02^{+1.24}_{-1.06}$ km [126].

From our results, the M-R diagram of the initial conditions for fixed T ($T = 5$ MeV) and fixed $S/n_b = 1 k_B$ overlap, similar to their M_{\max} 's on Table I, and are also marked with red dots on the curves. On the other hand, the M-R diagram of $T = 50$ MeV NS remnant matter has the largest size with relatively small M_{\max} compared to the $S/n_b = 6 k_B$ NS remnant matter with the highest M_{\max} even though it's core temperature is higher than 50 MeV. Hence, fixed S/n_b NS remnants appear more compact than fixed T NS remnants. Additionally, we observed that the mass and radius of the remnant increase with an increasing S/n_b . In the case of prompt black hole formation, the remnant mass also increases with increasing lepton number and S/n_b . Analysing Figs. 1 and 3 together with the M-R diagram, we can deduce that fewer neutrino content (particularly ν_e) and early appearance of the μ and s -quark in the remnant matter reduces its pressure thereby softening the EoS and consequently, reducing the maximum mass and radii. On the other hand, the existence of NSs with a larger mass and radius when increasing T or S/n_b are indeed a consequence of the enhancement of the strength of the term proportional to $n_b^{1/3}$ in the equivalent quark mass when T increases towards T_C .

In Fig. 7, we show the result of the square of sound velocity, c_s^2 as a function of the n_b/n_0 . The c_s^2 is determined using the EoS as inputs from the expression

$$c_s^2 = \frac{\partial P}{\partial \varepsilon}, \quad (46)$$

where c_s is measured in the unit of constant speed of light (c). The c_s helps to distinguish between the properties of strongly interacting matter using conformal symmetry arguments and more importantly measure the stiff-

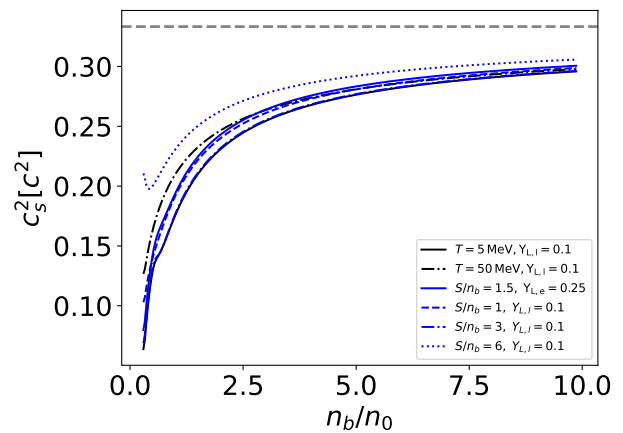


FIG. 7. The sound velocity through the NS remnant matter as a function of n_b/n_0 . The horizontal gray line represents the conformal limit, $c_s^2 = 1/3$, above this limit matter is considered to be in a hadronic state, and below it, matter is considered asymptotically free.

ness of the EoS. The confined matter (hadron) phase is not conformally symmetric due to chiral symmetry breaking, but the deconfined QM phase, on the other hand, is conformally symmetric due to asymptotic freedom. The matter is classified as exactly symmetric under conformal transformation when $c_s^2 = 1/3$, in highly dense free QM ($n_b > 40 n_0$) this limit, is approached from below [127] due to quark deconfinement, asymptotic freedom, and small quark masses. The c_s is estimated to be $c_s^2 \gtrsim 0.5$ in hadronic matter, it must also satisfy causality constraint $c_s^2 \leq 1$, and thermodynamic stability condition $c_s^2 > 0$ for all kinds of matter compositions [128]. It is an important parameter for determining quark core in massive NSs (i.e. hybrid NSs) [38, 49] and for determining the behavior of QM that form QSs [34], whether the quarks behave as being confined or free. The results above show that the c_s is higher in high S/n_b remnant matter, in general. Hence, more massive remnants are associated with high c_s than less massive ones. However, in the case of larger sized and less compact remnants (we are comparing $T = 50$ MeV and $S/n_b = 6 k_B$) the c_s is relatively higher at low n_b and falls slightly as n_b increases. The small tail seen in the $S/n_b = 6 k_B$ curve at low n_b is due to the different behavior of the u and d -quarks at this entropy (see Fig. 3), in that region. They show a sharp rise at low n_b and start decreasing steadily relative to their behavior in other stages of the remnant evolution. Comparing the c_s curves to the particle distributions in Figs. 1 and 3, we can infer that the ν_e has a significant impact on the c_s in the remnant matter. The early appearance of ν_e in the remnant shows higher c_s at low n_b and a higher rise of ν_e toward the center of the remnant results in higher c_s at higher n_b .

In Fig. 8, we show the polytropic index as a function

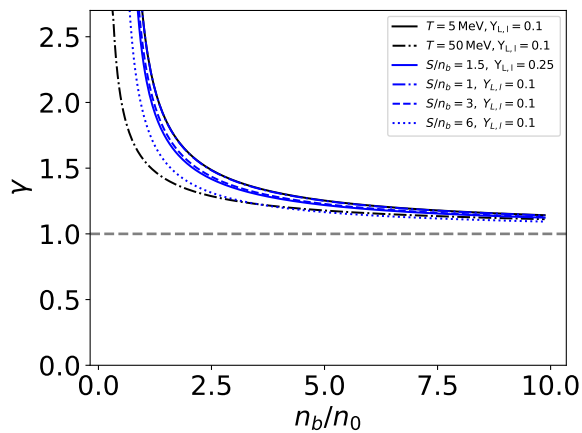


FIG. 8. The polytropic index as a function of n_b/n_0 . The horizontal gray line is the conformal limit $\gamma = 1$.

of n_b/n_0 determined through the relation

$$\gamma = \frac{\partial \ln P}{\partial \ln \varepsilon}, \quad (47)$$

using the EoS as input. The γ is also used to classify the inner composition and the forms of matter in the NS remnant matter. The application of the γ is similar to the c_s discussed above. They constitute the two most important parameters for determining the classes of matter that form an NS or exist in the core of the NS (if the existence of a hybrid NS is assumed [38]) using the EoS. A conformally symmetric matter is scale-independent and does not involve any dimensionful parameter, therefore, P and ε are expected to be proportional given rise to $\gamma = 1$. On the contrary, the value of γ in the hadronic matter, for instance, is estimated to be $\gamma \approx 2.5$ around and above the n_0 in chiral effective theories, setting a threshold for classifying hadrons and free quark matter [127, 129]. This is expected because the ground state of the QCD theory does not have its usual approximate chiral symmetry at low to intermediate baryon densities [130]. From Fig. 8, we observe that γ decreases as n_b increases and attains its minimum value $\gamma \approx 1.1$ at the high-density region. This value is slightly above the conformal limit (the horizontal gray line), however, it is in good agreement with conformal matter classification, comparing this results to the new limit set in [38] after examining a wide range of EoSs, estimating it at $\gamma \leq 1.75$. Additionally, we observe that heavier remnants approach the $\gamma = 1$ threshold faster than less massive remnants.

IV. FINAL REMARKS

We studied the BNS postmerger remnants in the presence of e and μ and their corresponding neutrinos, assuming that the merger remnant is a neutron star composed of self-bound free quarks, using DDQM. Generally, the aftermath of the merger has three different out-

comes; 1) it may form a stable NS, 2) form a black hole, or 3) a supramassive rotationally supported NS, which will later collapse to form a black hole due to angular momentum losses. The possibility of any of these three scenarios occurring depends on the masses and the EoSs of the NS binaries participating in the merger event. In each scenario, the event will affect the GW signal and its electromagnetic counterpart (see Refs. [119, 131, 132] for more detailed discussions). Assuming a stable NS was formed in the framework of this study, a few seconds after the merger, the remnant will go through deleptonization, neutrino diffusion, and thermal radiations to form a stable strange quark star (SQS) at $T = 0$, several years later. In that case, the $M_{\max} = 2.18M_{\odot}$ and the radius $R = 13.86\text{km}$ with dimensionless tidal deformability parameter $\Lambda_{1.4} = 2163$, as shown on Table II of [34]. Hence, as the remnant cools down it shrinks, and its mass and radius decrease as compared to the hotter counterparts. That notwithstanding, the model strongly violates the $\Lambda_{1.4}$ extracted from the GW170817 event with an upper bound of $\Lambda_{1.4} \leq 800$. However, this seems to be a problem with most of the phenomenological quark models used to study SQSs; a similar extreme violation of the $\Lambda_{1.4}$ was found in [133] using a confining quark model and in [73] using quasiparticle model. These violations may be a result of higher radii beyond the $\sim 13\text{km}$ threshold generated by these models to achieve the $2M_{\odot}$ minimum threshold as projected in [134]. The violation suggests that the two NS binaries that were involved in the merger event that led to the observation of the GW170817 might not be quark stars.

The main findings of our investigation are:

- In the upper panels of Fig. 1 and in Fig. 3 we observed a significant increase in ν_e as the merger remnant evolves with increasing T and S/n_b . The ν_e 's shift more towards the low n_b region and their population also increases significantly toward the center of the remnant matter along the evolution lines. The ν_{μ} population drops marginally at low n_b and does not show any significant increase at higher n_b along the evolution lines. The δ of the remnant matter also decreases with increasing T and S/n_b due to excess u over d -quarks along the evolution lines. As expected, an increase in T and S/n_b facilitates the early appearance of s -quark in the remnant matter, a similar effect was observed with the μ 's. Particle distribution under conditions of merger involving hadronic matter can be found in [115, 135], their results qualitatively agree with our findings considering that neutrons are rich in u , protons are rich in d and hyperons contain s -quarks.
- In the lower panels of Fig. 1, we found that massless particles like ν_e and ν_{μ} contribute less to the overall S/n_b of the system. Generally, an increase in T mutually increases the S/n_b of each particle in the system thereby increasing the net S/n_b as

shown in Fig. 2. Additionally, the S/n_b decreases with increasing n_b among the individual particles, a similar effect is observed in the net system of particles in Fig. 2. This reinforces the point that the S/n_b spreads from the disk towards the center of the remnants (higher S/n_b in the time interval of ~ 40 ms postmerger have been reported in [118]).

- In Fig. 4, we found that a delayed appearance of the s -quark and μ in the remnant matter coupled with a large δ soften the EoS resulting into lower M_{\max} and R . On the other hand, a shift of the ν_e towards the low n_b region increases the pressure in the remnant matter and stiffens the EoS leading to higher M_{\max} and R . The ν_μ constituent does not significantly affect the EoS along the evolution lines however, its marginal decrease at low n_b and marginal increase at higher n_b coincides with the stiffening of the EoS as the remnant evolves. Generally, we observed that the remnants' EoS becomes stiffer as T and S/n_b increase, as a result of the $n_b^{1/3}$ dependence of the equivalent quark mass and the enhancement of this term by driving T to the critical deconfinement temperature.
- We observed a connection between temperature rise, neutrino production, and the emergence of different particles in the remnant matter. The matter with the highest temperature profile in Fig. 5 corresponds to the matter with the highest neutrino content, particularly ν_e , early appearance of s and μ , and less δ . We find that the temperature increases with n_b and higher values of S/n_b , reaching core temperatures ranging between $T_c \sim 9 - 51$ MeV along the evolution lines considered. These values are within the lower limits reported in Refs. [12, 112, 116] for postmerger remnant matter. Temperature increases in the remnant reduce both the central energy and baryon densities. It should be noted that temperatures in quark matter are generally lower than a corresponding hadronic matter investigated under the same conditions due to a higher degeneracy in quark matter.
- The EoSs calculated and analyzed produced non-rotating spherically symmetric static compact objects with maximum masses of between $2.25 - 2.67M_\odot$, which is fairly in agreement with the estimated combined masses of the NS binaries that were involved in the GW170817 event [1] and the secondary component in the GW190814 event with maximum mass of $2.59_{-0.09}^{+0.08}M_\odot$ [136]. The maximum masses also satisfy the threshold set by

PSR J0740+6620, and the remnant radii determined are within the upper limits of the radius determined for PSR J0740+6620 by [125] through the analyses of the NICER observatory data (see the result in Fig. 6 and Table I). Since the maximum masses obtained here are higher than the ones obtained for PSR J0740+6620, even though their radii correspond to the upper limit, we can infer that the NS remnants analyzed here are more compact. Besides, the results satisfy the maximum NS mass constraints set through more massive PSR J2215+5135 [137] and PSR J0952-0607 [67] observed pulsars.

- Finally, we analyzed the composition of the remnant matter through the conformal symmetry arguments using the EoS as input. The results obtained for c_s and γ are presented in Figs. 7 and 8 respectively. The graphs show $c_s^2 < 1/3$ and $\gamma \gtrsim 1.1$, in conformity with conformal matter classification detailed in [38] through a wide range of EoSs analyzed.

Consequently, we have established that the BNS merger remnant can be an SQS that satisfies the $2M_\odot$ constraint of NSs. The μ populations in the SQS remnant showed a significant variation as the remnant evolved, influencing the EoS temperature profile, and the macroscopic structure of the SQS remnant. On the other hand, we found from our calculations that the presence of the ν_μ increases the maximum mass of the NS remnants by approximately $\sim 0.94\%$ and radii by $\sim 0.75\%$, drops the central energy density by $\sim 0.086\%$, the baryon density by $\sim 0.41\%$ and almost $\sim 0.92\%$ drop in the core temperature as well. Also, the presence of ν_e in the remnant matter significantly influences the EoS along the evolution lines as compared to the ν_μ .

V. ACKNOWLEDGEMENTS

A.I. thanks the financial support from the São Paulo State Research Foundation (FAPESP) Grant No. 2023/09545-1. T. F. thanks the financial support from the Brazilian Institutions: National Council for Scientific and Technological Development CNPq (Grant No. 306834/2022-7), Improvement of Higher Education Personnel CAPES (Finance Code 001) and FAPESP (Grants No. 2017/05660-0 and 2019/07767-1). This work is a part of the project Instituto Nacional de Ciência e Tecnologia - Física Nuclear e Aplicações Proc. No. 464898/2014-5.

[1] B. P. Abbott *et al.*, “GW170817: Observation of Gravitational Waves from a Binary Neutron Star Inspiral,”

Phys. Rev. Lett., vol. 119, no. 16, p. 161101, 2017.

- [2] L. Baiotti and L. Rezzolla, “Binary neutron star mergers: a review of Einstein’s richest laboratory,” *Rept. Prog. Phys.*, vol. 80, no. 9, p. 096901, 2017.
- [3] L. Barack *et al.*, “Black holes, gravitational waves and fundamental physics: a roadmap,” *Class. Quant. Grav.*, vol. 36, no. 14, p. 143001, 2019.
- [4] K. Hotokezaka, K. Kyutoku, H. Okawa, M. Shibata, and K. Kiuchi, “Binary Neutron Star Mergers: Dependence on the Nuclear Equation of State,” *Phys. Rev. D*, vol. 83, p. 124008, 2011.
- [5] A. Bauswein, T. W. Baumgarte, and H. T. Janka, “Prompt merger collapse and the maximum mass of neutron stars,” *Phys. Rev. Lett.*, vol. 111, no. 13, p. 131101, 2013.
- [6] K. Hotokezaka, K. Kiuchi, K. Kyutoku, T. Muranushi, Y.-i. Sekiguchi, M. Shibata, and K. Taniguchi, “Remnant massive neutron stars of binary neutron star mergers: Evolution process and gravitational waveform,” *Phys. Rev. D*, vol. 88, p. 044026, 2013.
- [7] J. Aasi *et al.*, “Advanced LIGO,” *Class. Quant. Grav.*, vol. 32, p. 074001, 2015.
- [8] F. Acernese *et al.*, “Advanced Virgo: a second-generation interferometric gravitational wave detector,” *Class. Quant. Grav.*, vol. 32, no. 2, p. 024001, 2015.
- [9] B. P. Abbott *et al.*, “GW170817: Measurements of neutron star radii and equation of state,” *Phys. Rev. Lett.*, vol. 121, no. 16, p. 161101, 2018.
- [10] B. P. Abbott *et al.*, “Gravitational Waves and Gamma-rays from a Binary Neutron Star Merger: GW170817 and GRB 170817A,” *Astrophys. J. Lett.*, vol. 848, no. 2, p. L13, 2017.
- [11] A. Goldstein *et al.*, “An Ordinary Short Gamma-Ray Burst with Extraordinary Implications: Fermi-GBM Detection of GRB 170817A,” *Astrophys. J. Lett.*, vol. 848, no. 2, p. L14, 2017.
- [12] A. Perego, S. Bernuzzi, and D. Radice, “Thermodynamics conditions of matter in neutron star mergers,” *Eur. Phys. J. A*, vol. 55, no. 8, p. 124, 2019.
- [13] B. P. Abbott *et al.*, “Multi-messenger Observations of a Binary Neutron Star Merger,” *Astrophys. J. Lett.*, vol. 848, no. 2, p. L12, 2017.
- [14] B. P. Abbott *et al.*, “GW190425: Observation of a Compact Binary Coalescence with Total Mass $\sim 3.4M_{\odot}$,” *Astrophys. J. Lett.*, vol. 892, no. 1, p. L3, 2020.
- [15] M. Maggiore *et al.*, “Science Case for the Einstein Telescope,” *JCAP*, vol. 03, p. 050, 2020.
- [16] B. P. Abbott *et al.*, “Exploring the Sensitivity of Next Generation Gravitational Wave Detectors,” *Class. Quant. Grav.*, vol. 34, no. 4, p. 044001, 2017.
- [17] B. P. Abbott *et al.*, “Prospects for observing and localizing gravitational-wave transients with Advanced LIGO, Advanced Virgo and KAGRA,” *Living Rev. Rel.*, vol. 21, no. 1, p. 3, 2018.
- [18] M. Shibata and K. Uryu, “Simulation of merging binary neutron stars in full general relativity: Gamma = two case,” *Phys. Rev. D*, vol. 61, p. 064001, 2000.
- [19] Y. Sekiguchi, K. Kiuchi, K. Kyutoku, and M. Shibata, “Effects of hyperons in binary neutron star mergers,” *Phys. Rev. Lett.*, vol. 107, p. 211101, 2011.
- [20] S. Bernuzzi, D. Radice, C. D. Ott, L. F. Roberts, P. Moesta, and F. Galeazzi, “How loud are neutron star mergers?,” *Phys. Rev. D*, vol. 94, no. 2, p. 024023, 2016.
- [21] D. Radice, A. Perego, K. Hotokezaka, S. A. Fromm, S. Bernuzzi, and L. F. Roberts, “Binary Neutron Star Mergers: Mass Ejection, Electromagnetic Counterparts and Nucleosynthesis,” *Astrophys. J.*, vol. 869, no. 2, p. 130, 2018.
- [22] A. Bauswein, H. T. Janka, and R. Oechslin, “Testing Approximations of Thermal Effects in Neutron Star Merger Simulations,” *Phys. Rev. D*, vol. 82, p. 084043, 2010.
- [23] S. Rosswog, T. Piran, and E. Nakar, “The multi-messenger picture of compact object encounters: binary mergers versus dynamical collisions,” *Mon. Not. Roy. Astron. Soc.*, vol. 430, p. 2585, 2013.
- [24] L. F. Roberts, G. Shen, V. Cirigliano, J. A. Pons, S. Reddy, and S. E. Woosley, “Protoneutron star cooling with convection: The effect of the symmetry energy,” *Physical Review Letters*, vol. 108, no. 6, p. 061103, 2012.
- [25] A. Issifu, F. M. da Silva, and D. P. Menezes, “Protostrange quark stars from density-dependent quark mass model,” 11 2023.
- [26] M. Shibata and K. Taniguchi, “Coalescence of Black Hole-Neutron Star Binaries,” *Living Rev. Rel.*, vol. 14, p. 6, 2011.
- [27] J. A. Faber and F. A. Rasio, “Binary Neutron Star Mergers,” *Living Rev. Rel.*, vol. 15, p. 8, 2012.
- [28] S. Rosswog, “The multi-messenger picture of compact binary mergers,” *Int. J. Mod. Phys. D*, vol. 24, no. 05, p. 1530012, 2015.
- [29] M. Prakash, I. Bombaci, M. Prakash, P. J. Ellis, J. M. Lattimer, and R. Knorren, “Composition and structure of protoneutron stars,” *Phys. Rept.*, vol. 280, pp. 1–77, 1997.
- [30] H.-T. Janka, K. Langanke, A. Marek, G. Martinez-Pinedo, and B. Mueller, “Theory of Core-Collapse Supernovae,” *Phys. Rept.*, vol. 442, pp. 38–74, 2007.
- [31] D. D. Ivanenko and D. F. Kurdgelaidze, “Hypothesis concerning quark stars,” *Astrophysics*, vol. 1, pp. 251–252, 1965.
- [32] D. D. Ivanenko and D. F. Kurdgelaidze, “Quark stars,” *Sov. Phys. J.*, vol. 13, pp. 1015–1019, 1970.
- [33] E. Witten, “Cosmic Separation of Phases,” *Phys. Rev. D*, vol. 30, pp. 272–285, 1984.
- [34] F. M. da Silva, A. Issifu, L. L. Lopes, L. C. N. Santos, and D. P. Menezes, “A Bayesian study of quark models in view of recent astrophysical constraints,” 2023.
- [35] A. R. Bodmer, “Collapsed nuclei,” *Phys. Rev. D*, vol. 4, pp. 1601–1606, Sep 1971.
- [36] I. Bombaci, I. Parenti, and I. Vidana, “Quark deconfinement and implications for the radius and the limiting mass of compact stars,” *Astrophys. J.*, vol. 614, pp. 314–325, 2004.
- [37] M. Herzog and F. K. Ropke, “Three-dimensional hydrodynamic simulations of the combustion of a neutron star into a quark star,” *Phys. Rev. D*, vol. 84, p. 083002, 2011.
- [38] E. Annala, T. Gorda, A. Kurkela, J. Nättilä, and A. Vuorinen, “Evidence for quark-matter cores in massive neutron stars,” *Nature Phys.*, vol. 16, no. 9, pp. 907–910, 2020.
- [39] B. P. Abbott *et al.*, “Observation of Gravitational Waves from a Binary Black Hole Merger,” *Phys. Rev. Lett.*, vol. 116, no. 6, p. 061102, 2016.
- [40] T. E. Riley *et al.*, “A *NICER* View of PSR J0030+0451: Millisecond Pulsar Parameter Estimation,” *Astrophys. J. Lett.*, vol. 887, no. 1, p. L21, 2019.

- [41] H. T. Cromartie *et al.*, “Relativistic Shapiro delay measurements of an extremely massive millisecond pulsar,” *Nature Astron.*, vol. 4, no. 1, pp. 72–76, 2019.
- [42] E. Fonseca *et al.*, “Refined Mass and Geometric Measurements of the High-mass PSR J0740+6620,” *Astrophys. J. Lett.*, vol. 915, no. 1, p. L12, 2021.
- [43] T. E. Riley *et al.*, “A NICER View of the Massive Pulsar PSR J0740+6620 Informed by Radio Timing and XMM-Newton Spectroscopy,” *Astrophys. J. Lett.*, vol. 918, no. 2, p. L27, 2021.
- [44] K. D. Marquez, D. P. Menezes, H. Pais, and C. Providência, “ Δ baryons in neutron stars,” *Phys. Rev. C*, vol. 106, no. 5, p. 055801, 2022.
- [45] A. Issifu, K. D. Marquez, M. R. Pelicer, and D. P. Menezes, “Exotic baryons in hot neutron stars,” *Mon. Not. Roy. Astron. Soc.*, vol. 522, no. 3, pp. 3263–3270, 2023.
- [46] V. B. Thapa, A. Kumar, and M. Sinha, “Baryonic dense matter in view of gravitational-wave observations,” *Mon. Not. Roy. Astron. Soc.*, vol. 507, no. 2, pp. 2991–3004, 2021.
- [47] L. Bonanno and A. Sedrakian, “Composition and stability of hybrid stars with hyperons and quark color-superconductivity,” *Astron. Astrophys.*, vol. 539, p. A16, 2012.
- [48] A. Kumar, V. B. Thapa, and M. Sinha, “Hybrid stars are compatible with recent astrophysical observations,” *Phys. Rev. D*, vol. 107, no. 6, p. 063024, 2023.
- [49] A. Issifu, F. M. da Silva, and D. P. Menezes, “Hybrid stars built with density-dependent models,” *Mon. Not. Roy. Astron. Soc.*, vol. 525, no. 4, pp. 5512–5519, 2023.
- [50] D. Ivanenko and D. F. Kurdgelaidze, “Remarks on quark stars,” *Lett. Nuovo Cim.*, vol. 2, pp. 13–16, 1969.
- [51] N. Itoh, “Hydrostatic Equilibrium of Hypothetical Quark Stars,” *Prog. Theor. Phys.*, vol. 44, p. 291, 1970.
- [52] C. Alcock, E. Farhi, and A. Olinto, “Strange stars,” *Astrophysical Journal, Part 1 (ISSN 0004-637X)*, vol. 310, Nov. 1, 1986, p. 261–272., vol. 310, pp. 261–272, 1986.
- [53] V. K. Gupta, A. Gupta, S. Singh, and J. D. Anand, “Study of proto strange stars (pss) in temperature and density dependent quark mass model,” *Int. J. Mod. Phys. D*, vol. 12, pp. 583–595, 2003.
- [54] J. Shen, Y. Zhang, B. Wang, and R.-K. Su, “Slowly rotating proto strange stars in quark mass density-and temperature-dependent model,” *International Journal of Modern Physics A*, vol. 20, no. 32, pp. 7547–7565, 2005.
- [55] V. Dexheimer, J. R. Torres, and D. P. Menezes, “Stability windows for proto-quark stars,” *Eur. Phys. J. C*, vol. 73, p. 2569, 2013.
- [56] V. Dexheimer, D. P. Menezes, and M. Strickland, “The influence of strong magnetic fields on proto-quark stars,” *J. Phys. G*, vol. 41, p. 015203, 2014.
- [57] A. Drago, A. Lavagno, and G. Pagliara, “Can very compact and very massive neutron stars both exist?,” *Phys. Rev. D*, vol. 89, no. 4, p. 043014, 2014.
- [58] A. Drago and G. Pagliara, “The scenario of two families of compact stars: Part 2: Transition from hadronic to quark matter and explosive phenomena,” *The European Physical Journal A*, vol. 52, pp. 1–15, 2016.
- [59] C. Kettner, F. Weber, M. K. Weigel, and N. K. Glendenning, “Structure and stability of strange and charm stars at finite temperatures,” *Physical Review D*, vol. 51, no. 4, p. 1440, 1995.
- [60] V. V. Usov, “Low-mass normal-matter atmospheres of strange stars and their radiation,” *The Astrophysical Journal*, vol. 481, no. 2, p. L107, 1997.
- [61] D. B. Melrose, R. Fok, and D. P. Menezes, “Pair emission from bare magnetized strange stars,” *Monthly Notices of the Royal Astronomical Society*, vol. 371, no. 1, pp. 204–210, 2006.
- [62] G. X. Peng, H. C. Chiang, J. J. Yang, L. Li, and B. Liu, “Mass formulas and thermodynamic treatment in the mass density dependent model of strange quark matter,” *Phys. Rev. C*, vol. 61, p. 015201, 2000.
- [63] E. Eichten, K. Gottfried, T. Kinoshita, J. Kogut, K. D. Lane, and T. M. Yan, “Spectrum of charmed quark-antiquark bound states,” *Phys. Rev. Lett.*, vol. 34, pp. 369–372, Feb 1975.
- [64] G. S. Bali, “QCD forces and heavy quark bound states,” *Phys. Rept.*, vol. 343, pp. 1–136, 2001.
- [65] S. Afonin and T. Solomko, “Cornell potential in generalized soft wall holographic model,” *J. Phys. G*, vol. 49, no. 10, p. 105003, 2022.
- [66] E. S. Fraga, A. Kurkela, and A. Vuorinen, “Interacting quark matter equation of state for compact stars,” *The Astrophysical Journal Letters*, vol. 781, no. 2, p. L25, 2014.
- [67] R. W. Romani, D. Kandel, A. V. Filippenko, T. G. Brink, and W. Zheng, “PSR J0952–0607: The Fastest and Heaviest Known Galactic Neutron Star,” *Astrophys. J. Lett.*, vol. 934, no. 2, p. L17, 2022.
- [68] G.-y. Huang and S. Zhou, “Precise Values of Running Quark and Lepton Masses in the Standard Model,” *Phys. Rev. D*, vol. 103, no. 1, p. 016010, 2021.
- [69] Z.-z. Xing, H. Zhang, and S. Zhou, “Updated Values of Running Quark and Lepton Masses,” *Phys. Rev. D*, vol. 77, p. 113016, 2008.
- [70] Z. Zhang, P.-C. Chu, X.-H. Li, H. Liu, and X.-M. Zhang, “Quark matter and quark stars in a quasiparticle model,” *Phys. Rev. D*, vol. 103, no. 10, p. 103021, 2021.
- [71] B. C. Backes, E. Hafemann, I. Marzola, and D. P. Menezes, “Density dependent quark mass model revisited: Thermodynamic consistency, stability windows and stellar properties,” *J. Phys. G*, vol. 48, no. 5, p. 055104, 2021.
- [72] X. J. Wen, X. H. Zhong, G. X. Peng, P. N. Shen, and P. Z. Ning, “Thermodynamics with density and temperature dependent particle masses and properties of bulk strange quark matter and strangelets,” *Phys. Rev. C*, vol. 72, p. 015204, 2005.
- [73] P.-C. Chu, Y.-Y. Jiang, H. Liu, Z. Zhang, X.-M. Zhang, and X.-H. Li, “Quark star matter at finite temperature in a quasiparticle model,” *The European Physical Journal C*, vol. 81, pp. 1–9, 2021.
- [74] K. Schertler, C. Greiner, and M. H. Thoma, “Medium effects in strange quark matter and strange stars,” *Nucl. Phys. A*, vol. 616, pp. 659–679, 1997.
- [75] A. Peshier, B. Kampfer, and G. Soff, “The Equation of state of deconfined matter at finite chemical potential in a quasiparticle description,” *Phys. Rev. C*, vol. 61, p. 045203, 2000.
- [76] F. G. Gardim and F. M. Steffens, “Thermodynamics of Quasi-Particles at Finite Chemical Potential,” *Nucl. Phys. A*, vol. 825, pp. 222–244, 2009.
- [77] G. N. Fowler, S. Raha, and R. M. Weiner, “Confinement and Phase Transitions,” *Z. Phys. C*, vol. 9, p. 271, 1981.

- electron scattering,” *Phys. Rev. C*, vol. 102, no. 4, p. 044321, 2020.
- [114] Y. Sekiguchi, K. Kiuchi, K. Kyutoku, and M. Shibata, “Dynamical mass ejection from binary neutron star mergers: Radiation-hydrodynamics study in general relativity,” *Phys. Rev. D*, vol. 91, no. 6, p. 064059, 2015.
- [115] A. Sedrakian and A. Harutyunyan, “Equation of State and Composition of Proto-Neutron Stars and Merger Remnants with Hyperons,” *Universe*, vol. 7, no. 10, p. 382, 2021.
- [116] E. R. Most, A. Motornenko, J. Steinheimer, V. Dexheimer, M. Hanauske, L. Rezzolla, and H. Stoecker, “Probing neutron-star matter in the lab: Similarities and differences between binary mergers and heavy-ion collisions,” *Phys. Rev. D*, vol. 107, no. 4, p. 043034, 2023.
- [117] M. Prakash, J. M. Lattimer, J. A. Pons, A. W. Steiner, and S. Reddy, “Evolution of a neutron star from its birth to old age,” *Lect. Notes Phys.*, vol. 578, pp. 364–423, 2001.
- [118] A. Perego, S. Rosswog, R. M. Cabezón, O. Korobkin, R. Käppeli, A. Arcones, and M. Liebendörfer, “Neutrino-driven winds from neutron star merger remnants,” *Mon. Not. Roy. Astron. Soc.*, vol. 443, no. 4, pp. 3134–3156, 2014.
- [119] D. Radice, S. Bernuzzi, and A. Perego, “The Dynamics of Binary Neutron Star Mergers and GW170817,” *Ann. Rev. Nucl. Part. Sci.*, vol. 70, pp. 95–119, 2020.
- [120] J. R. Oppenheimer and G. M. Volkoff, “On Massive Neutron Cores,” *Physical Review*, vol. 55, pp. 374–381, Feb 1939.
- [121] T. M. Tauris *et al.*, “Formation of Double Neutron Star Systems,” *Astrophys. J.*, vol. 846, no. 2, p. 170, 2017.
- [122] L. Bildsten and C. Cutler, “Tidal Interactions of Inspiral Compact Binaries,” *Astrophys. J.*, vol. 400, p. 175, Nov. 1992.
- [123] F. Özel, D. Psaltis, R. Narayan, and J. E. McClintock, “The black hole mass distribution in the galaxy,” *The Astrophysical Journal*, vol. 725, no. 2, p. 1918, 2010.
- [124] L. Kreidberg, C. D. Bailyn, W. M. Farr, and V. Kalogera, “Mass measurements of black holes in x-ray transients: Is there a mass gap?,” *The Astrophysical Journal*, vol. 757, no. 1, p. 36, 2012.
- [125] M. C. Miller *et al.*, “The Radius of PSR J0740+6620 from NICER and XMM-Newton Data,” *Astrophys. J. Lett.*, vol. 918, no. 2, p. L28, 2021.
- [126] M. C. Miller *et al.*, “PSR J0030+0451 Mass and Radius from NICER Data and Implications for the Properties of Neutron Star Matter,” *Astrophys. J. Lett.*, vol. 887, no. 1, p. L24, 2019.
- [127] A. Kurkela, P. Romatschke, and A. Vuorinen, “Cold Quark Matter,” *Phys. Rev. D*, vol. 81, p. 105021, 2010.
- [128] P. Bedaque and A. W. Steiner, “Sound velocity bound and neutron stars,” *Phys. Rev. Lett.*, vol. 114, no. 3, p. 031103, 2015.
- [129] H. Liu, X.-M. Zhang, and P.-C. Chu, “Properties of quark-matter cores in massive hybrid stars,” *Phys. Rev. D*, vol. 107, no. 9, p. 094032, 2023.
- [130] J. W. Holt, N. Kaiser, and W. Weise, “Density-dependent effective nucleon-nucleon interaction from chiral three-nucleon forces,” *Phys. Rev. C*, vol. 81, p. 024002, 2010.
- [131] N. Sarin and P. D. Lasky, “The evolution of binary neutron star post-merger remnants: a review,” *Gen. Rel. Grav.*, vol. 53, no. 6, p. 59, 2021.
- [132] A. L. Piro, B. Giacomazzo, and R. Perna, “The Fate of Neutron Star Binary Mergers,” *Astrophys. J. Lett.*, vol. 844, no. 2, p. L19, 2017.
- [133] Z. Cao, L.-W. Chen, P.-C. Chu, and Y. Zhou, “GW190814: Circumstantial evidence for up-down quark star,” *Phys. Rev. D*, vol. 106, no. 8, p. 083007, 2022.
- [134] C. Raithel, F. Özel, and D. Psaltis, “Tidal deformability from GW170817 as a direct probe of the neutron star radius,” *Astrophys. J. Lett.*, vol. 857, no. 2, p. L23, 2018.
- [135] A. Sedrakian and A. Harutyunyan, “Delta-resonances and hyperons in proto-neutron stars and merger remnants,” *Eur. Phys. J. A*, vol. 58, no. 7, p. 137, 2022.
- [136] R. Abbott *et al.*, “GW190814: Gravitational Waves from the Coalescence of a 23 Solar Mass Black Hole with a 2.6 Solar Mass Compact Object,” *Astrophys. J. Lett.*, vol. 896, no. 2, p. L44, 2020.
- [137] M. Linares, T. Shahbaz, and J. Casares, “Peering into the dark side: Magnesium lines establish a massive neutron star in PSR J2215+5135,” *Astrophys. J.*, vol. 859, no. 1, p. 54, 2018.